



Facilitation of the visible light-induced Fenton-like excitation of H₂O₂ via heterojunction of g-C₃N₄/NH₂-Iron terephthalate metal-organic framework for MB degradation

Xiyi Li, Yunhong Pi, Liqiong Wu, Qibin Xia, Junliang Wu, Zhong Li, Jing Xiao *

School of Chemistry and Chemical Engineering, and Guangdong Provincial Key Laboratory of Atmospheric Environment and Pollution Control, South China University of Technology, Guangzhou 510640, PR China



ARTICLE INFO

Article history:

Received 16 July 2016

Received in revised form

25 September 2016

Accepted 30 September 2016

Available online 1 October 2016

Keywords:

NH₂-MIL-88B(Fe)

g-C₃N₄

Heterojunction

Fenton-like reaction

Photocatalyst

ABSTRACT

g-C₃N₄/NH₂-Iron terephthalate metal-organic framework heterojunction for visible light-induced Fenton-like excitation of H₂O₂ for MB degradation was investigated in this work. The g-C₃N₄/NH₂-MIL-88B(Fe) (namely lp-x composite) was hydrothermally synthesized and characterized by powder X-ray diffraction, Fourier transform infrared spectroscopy, X-ray photoelectron spectroscopy, transmission electron microscopy, UV-vis diffused reflectance spectroscopy, spin-trapping electron paramagnetic resonance and photoluminescence analysis. 100% of MB photodegradation was achieved by the lp-2 in 120 min under visible light, much greater than the parent g-C₃N₄ and NH₂-MIL-88B(Fe), individually. The synergistic index in the lp-2/visible-light/H₂O₂ system reached as high as 305%. The excitation of H₂O₂ over the lp-2 composite is clarified to go through (i) the direct and (ii) the photo-induced Fenton-like reactions, while the latter is greatly facilitated by the formation of the g-C₃N₄/NH₂-MIL-88B(Fe) heterojunction. In the lp-2 composite, the photoelectron transfers efficiently from the CB of g-C₃N₄ to NH₂-MIL-88B(Fe) for enhanced Fenton-like excitation of H₂O₂, rather than eliminates through e⁻-h⁺ pair recombination on g-C₃N₄, verified by the photoluminescence analysis and electron spin resonance technique. This work demonstrates the first example of facilitating Fenton-like excitation of H₂O₂ via introduction of g-C₃N₄ to stable amine functionalized Fe-centered MOF for visible light-induced photodegradation.

© 2016 Elsevier B.V. All rights reserved.

1. Introduction

More than 100,000 types of organic dyes with over 7×10^5 ton in total are produced annually in industry, which was however, highly toxic and hard to be biodegraded in nature [1,2]. These organic dyes can be potential hazards to the environment and human health, when getting into the water system in particular. Therefore, developing effective technology to degrade organic dyes from wastewater has been considered as an important task for a sustainable society.

Advanced oxidation processes (AOPs) show promises in the degradation of organic dyes, because of their high efficiency, simplicity, good regenerability, and easy handling [3,4]. Among various AOPs, visible light induced heterogeneous Fenton-like photocatalytic process has been considered as an effective method to degrade a series of organic dyes into easily degradable compounds [3,5–10]. In such process, highly reactive hydroxyl radical (•OH)

plays a critical role to degrade the contaminants [11], which is realized via the excitation of H₂O₂ using iron ions, e.g., Fe²⁺, Fe³⁺ [12]. However, most of currently developed processes are limited by rigorous pH range, long operation time and large energy consumption [13–15]. Therefore, further development of visible light induced efficient heterogeneous Fenton-like photocatalytic system is worthy of further exploration.

Metal-organic frameworks (MOFs), made up of metal ions and organic linkers, emerged as a new type of inorganic/organic hybrid crystals with tunable textural properties and functionalities [16]. MOFs show potential in gas storage and separation, drug delivery, sensing as well as catalysis [17–19]. Besides, owing to the unique metal-ligand coordination structure to form ligand-to-metal charge transfer (LMCT) under light radiation [20,21], MOFs have been considered as a new type of photocatalysts recently. Wang et al. reported a highly selective benzene hydroxylation to phenol by MIL-100(Fe) and MIL-68(Fe) under visible light [22]. Sedigheh Abedi et al. demonstrated that the incorporation of amorphous TiO₂ in MOF enhanced the photocatalytic oxidation of benzylic alcohols under sunlight [23]. Among various types of MOFs reported, Fe-centered MOFs showed great potential as the

* Corresponding author.

E-mail addresses: cejingxiao@scut.edu.cn, jux12@psu.edu (J. Xiao).

photocatalyst [24,25] due to its special structure of iron complex as the repeating unit, resulting in powerful Fenton-like excitation of H_2O_2 for effective photocatalytic reaction in water purification under light irradiation. For example, Ai et. al reported a Fe-centered MIL-53(Fe) as a photocatalyst for the Fenton-like excitation of H_2O_2 for RhB degradation [26]. Maarten et al. reported different iron(III)-based MOFs containing $\text{Fe}_3\text{-}\mu_3\text{-oxo}$ clusters for visible-light-induced Fenton-like excitation of H_2O_2 for Rhodamine 6G degradation [27]. Meanwhile, as a new class of carbon materials, $\text{g-C}_3\text{N}_4$ has been highlighted as a semiconductor due to its visible-light-active characteristics with unique tri-s-triazine units [28]. As a metal-free photocatalyst, $\text{g-C}_3\text{N}_4$ has attracted increasing attention and been reported to possess the photocatalytic performance for water splitting, organic degradation and conversion of CO_2 [29]. The photocatalytic activities of $\text{g-C}_3\text{N}_4$ could be tuned by the structure, including nanostructure [30,31], electronic structure [32,33] and heterostructure engineering [34]. Among various modification procedures, the formation of heterostructure has become a common and easy strategy to lower the recombination of photo-induced $\text{e}^-\text{-h}^+$ pairs. The $\text{g-C}_3\text{N}_4$ has been introduced to other semiconductors, including TiO_2 [35], ZnO [36] and Fe_2O_3 [37–39], for promoting the separation of photo-induced carriers for enhanced photocatalytic activities. Moreover, Fe- $\text{g-C}_3\text{N}_4$ was reported to be loaded on zeolite to act as an effective heterogeneous catalyst [40]. Based on the above two types of excellent semiconductors, we hypothesize that if Fe-centered MOF was hybridized to $\text{g-C}_3\text{N}_4$ successfully to separate photo-induced carriers, its Fenton-like excitation of H_2O_2 may be amplified for effective photodegradation of organic contaminants. However, to best of our knowledge, such approach has not been reported in the literature.

Herein, we report a novel composite of $\text{g-C}_3\text{N}_4$ hybridized Fe-centered MOF as an effective Fenton-like photocatalyst for MB degradation. For the first time, $\text{g-C}_3\text{N}_4$ was hybridized into the stable NH_2 -functionalized MIL-88B(Fe) forming a stable $\text{g-C}_3\text{N}_4/\text{NH}_2\text{-MIL-88B(Fe)}$ composite (namely lp-x). The heterojunction was formed between $\text{NH}_2\text{-MIL-88B(Fe)}$ and $\text{g-C}_3\text{N}_4$ during the solvothermal process, which thus facilitated the transfer of photo-induced electrons to reduce the recombination rate of $\text{e}^-\text{-h}^+$ pairs and the Fenton-like activation of H_2O_2 for the degradation of MB irradiated by visible light. The resulting lp-x composites were investigated by XRD, FT-IR, XPS, TEM and UV-vis DRS spectroscopy. The MB degradation efficiency, kinetics and synergetic index of the lp-x composites were evaluated. Cyclic usage of the lp-x composite was reported additionally. On the basis of electron spin resonance (ESR) and Photoluminescence (PL) analysis, the mechanism of visible light induced Fenton-like activation of H_2O_2 over the lp-x composite for photodegradation was clarified.

2. Experimental

2.1. Chemicals

Ferric chloride, melamine, 2-aminoterephthalic acid, N,N-dimethyl-formamide (DMF), methanol (MeOH), ethanol (EtOH), Hydrogen Peroxide (30%, v/v), and methylene blue dye (MB) were purchased from Alfa Aesar. All chemicals were of commercially available analytical grade and used without further purification.

2.2. Synthesis of $\text{g-C}_3\text{N}_4/\text{NH}_2\text{-MIL-88B(Fe)}$

2.2.1. Synthesis of $\text{g-C}_3\text{N}_4$

$\text{g-C}_3\text{N}_4$ was prepared following the previous report [41]. Typically, The melamine is heating in a crucible to 550 °C for 4 h under air.

2.2.2. Synthesis of $\text{NH}_2\text{-MIL-88B(Fe)}$

$\text{NH}_2\text{-MIL-88B(Fe)}$ was synthesized by a solvothermal process [42]. Generally, 1.1285 g of FeCl_3 , 0.7514 g H_2O and 1.8901 g 2-aminoterephthalic acid were added into 70 mL DMF solution. The solution stirred at room temperature for 30 min. Subsequently, the mixture was retained at 150 °C for 3 days in a Teflon-lined stainless steel autoclave (100 mL). After cooling, the slurry was centrifuged at 10,000 rpm for 3 min. The obtained brown products was washed with DMF and MeOH for three times, then were soaked in MeOH at 50 °C for 24 h in order to perform exchange of the guest solvent molecules with MeOH and collected by centrifugation. They were then dried at 80 °C for 24 h in a vacuum oven.

2.2.3. Synthesis of $\text{g-C}_3\text{N}_4/\text{NH}_2\text{-MIL-88B(Fe)}$

The synthesis of $\text{g-C}_3\text{N}_4/\text{NH}_2\text{-MIL-88B(Fe)}$ expect adding an appropriate amount of $\text{g-C}_3\text{N}_4$. The corresponding $\text{g-C}_3\text{N}_4/\text{NH}_2\text{-MIL-88B(Fe)}$ composites were designated as lp-x , $x = 1, 2, 3, 4$, following the added amount of $\text{g-C}_3\text{N}_4$ of 5, 10, 20, 30 wt.%.

2.3. Characterization

The powder X-ray diffraction (PXRD) measurements were carried out on a Bruker powder X-ray diffraction D8 Advance diffractometer with monochromatized $\text{Cu K}\alpha$ radiation ($\lambda = 0.15418 \text{ nm}$) source at 40 kV and 40 mA. The morphologies of the samples were investigated by transmission electron microscopy (TEM). The surface composition and chemical environment were analyzed by X-ray photoelectron spectroscopy (XPS, ESCALAB 250Xi), and the spectra was calibrated using the C 1s peak at 284.6 eV. The infrared absorption spectra was recorded using Nicolet 6700 FTIR Spectrometric Analyzer using KBr pel-lets. UV-vis diffused reflectance spectra of the samples were obtained on a UV-vis spectrophotometer (UV-3600, Shimadzu, Japan). BaSO_4 was chosen as a reflectance standard. Photoluminescence (PL) spectra of the as-prepared samples were obtained on a Hitachi F-4600 spectrometer with an excitation wavelength of 375 nm. Electron spin resonance (ESR) signals were measured on a JES FA200, (JEOL) electron paramagnetic resonance spectrometer under visible light.

2.4. Photocatalytic degradation experiments

The photocatalytic activities of $\text{NH}_2\text{-MIL-88B(Fe)}$, $\text{g-C}_3\text{N}_4$ and lp-x composites were investigated by the photodegradation of MB irradiated by a 500W Xe lamp with a 420 nm UV-cutoff filter under standard conditions (1 atm and 25 °C). The quartz tube with reactant mixtures was set 5 cm away from the light source. 0.050 g as-prepared sample was added into 50 mL of MB aqueous solution (30 mg/L) in a 60 mL cylindrical Pyrex vessel reactor. Before exposed to visible light, the suspension was magnetically stirred in the dark for 12 h to reach the adsorption/desorption equilibrium, 100 μL of known concentration of H_2O_2 was then added into the reactor and the lamp was turned on. The mixture of the suspension was stirred evenly during the MB photodegradation reaction. 2 mL of samples were withdrawn at regular intervals (30 min) with centrifugation to separate solids for measure.

2.5. Analytical methods

The MB concentration was analysed using a UV-vis spectrophotometer in a 1 cm path length spectrometric quartz cell to measure the absorption intensity at its maximum absorbance wavelength of 664 nm. The ESR signals of the trapped radical were recorded at ambient temperature on a JES FA200, (JEOL) spectrometer. All prepared mixtures (DMPO: 0.20 M, 20 μL + 0.5 mL water, sample: 10 mg) were added into a cylindrical quartz cell (length of 100 mm,

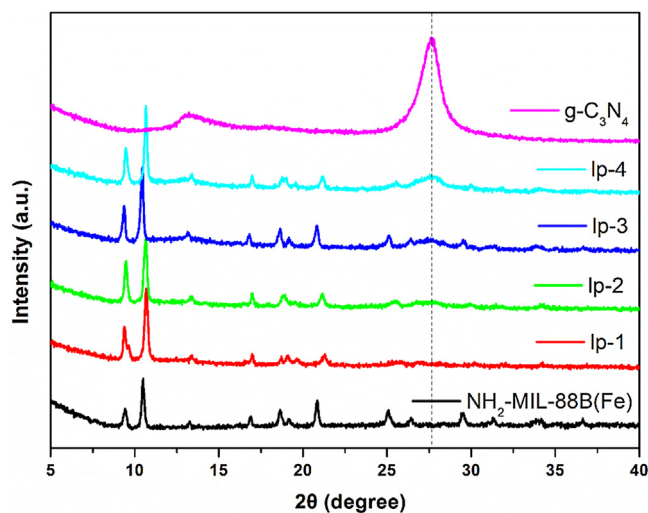


Fig. 1. XRD patterns of $\text{NH}_2\text{-MIL-88B(Fe)}$, $\text{g-C}_3\text{N}_4$ and lp-x composites.

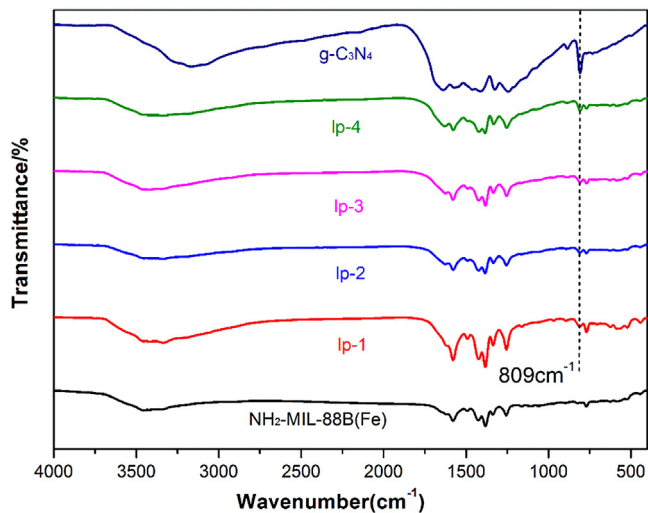


Fig. 2. FT-IR spectra of $\text{NH}_2\text{-MIL-88B(Fe)}$, $\text{g-C}_3\text{N}_4$ and lp-x composites.

diameter of 2 mm). A spot UV-vis light source (420 nm UV-cut off filter) was used in situ as a light source. The signals were taken every 2 min.

3. Results and discussion

3.1. Characterization

XRD patterns of the lp-x composites compared with the pristine $\text{NH}_2\text{-MIL-88B(Fe)}$ and $\text{g-C}_3\text{N}_4$ are shown in Fig. 1. The successful synthesis of $\text{NH}_2\text{-MIL-88B(Fe)}$ material was confirmed by the consistent XRD pattern of the parent $\text{NH}_2\text{-MIL-88B(Fe)}$ as those reported previously [43]. In comparison, the lp-x composites show similar XRD patterns as the parent $\text{NH}_2\text{-MIL-88B(Fe)}$, indicating the framework of $\text{NH}_2\text{-MIL-88B(Fe)}$ maintained after introducing C_3N_4 solvothermally. Meanwhile, a new peak at 27.2° appears in the XRD patterns of the lp-x composites, which can be assigned to the typical (002) interlayer-stacking peak from $\text{g-C}_3\text{N}_4$. Moreover, the characteristic peak of $\text{g-C}_3\text{N}_4$ becomes more evident by increasing the added amount of $\text{g-C}_3\text{N}_4$ in the lp-x composites.

FT-IR was carried out to identify the functionalities in the lp-x composites. Fig. 2 shows the FT-IR spectra of the lp-x composites referred to the parent $\text{NH}_2\text{-MIL-88B(Fe)}$ and $\text{g-C}_3\text{N}_4$. The charac-

teristic absorption peaks of $\text{g-C}_3\text{N}_4$ can be observed at 809 cm^{-1} corresponding to the stretching vibration of triazine cycles [44], which become stronger with increased mass content of $\text{g-C}_3\text{N}_4$ in lp-x composites, suggesting that $\text{g-C}_3\text{N}_4$ was successfully incorporated into the lp-x composites. For $\text{NH}_2\text{-MIL-88B(Fe)}$, the peaks at around 3385 and 3520 cm^{-1} [45], can be assigned to attributed to the symmetric and asymmetric stretching vibrations of amine N–H bonding in $\text{NH}_2\text{-MIL-88B(Fe)}$. In contrast, the bands were broadened after the incorporation of $\text{g-C}_3\text{N}_4$, which was likely ascribed to the additional N–H stretching vibration of $\text{g-C}_3\text{N}_4$ [44]. It should be mentioned that for the IR spectra of the lp-x composites, several characteristic peaks, such as C=N and C–N heterocycles skeletal vibrations of the aromatic ring from $\text{g-C}_3\text{N}_4$ were in the range of 1800 – 1400 cm^{-1} [44], which can be overlapped by the carbonyl (C=O) vibrations at about 1660 and 1700 cm^{-1} from $\text{NH}_2\text{-MIL-88B(Fe)}$ [46].

The morphology of the as-prepared samples was observed by TEM as displayed in Fig. 3. $\text{NH}_2\text{-MIL-88B(Fe)}$ crystals were spindle-shaped with a length of about $0.9\text{ }\mu\text{m}$ (Fig. 3a, b), similar as the previously reported literature [42]. The overlapping lamellar nanosheets were observed on the parent $\text{g-C}_3\text{N}_4$ (Fig. 3c, d), consistent with those reported in the literature [47]. For the lp-2 composite (Fig. 3e, f), it is noticed that smaller lamellar nanosheets were embedded into the almost spindle-shaped crystals, suggesting the successful incorporation of $\text{g-C}_3\text{N}_4$ into $\text{NH}_2\text{-MIL-88B(Fe)}$, and both parent structures were preserved after hybridization, consistent with the XRD and FT-IR results. The small particle size of $\text{g-C}_3\text{N}_4$ in the lp-x composites suggested that the $\text{g-C}_3\text{N}_4$ lamellar nanosheets can be highly embedded into $\text{NH}_2\text{-MIL-88B(Fe)}$ during the hydrothermal synthesis, and thus the formation of heterojunction between $\text{NH}_2\text{-MIL-88B(Fe)}$ and $\text{g-C}_3\text{N}_4$ was likely.

The information on chemical environment of the optimized lp-2 compared to the parent $\text{NH}_2\text{-MIL-88B(Fe)}$ were obtained in XPS analysis. The survey scanning spectrum as shown in Fig. 4(a) verified the presence of C, O, N and Fe in both samples. In comparison, the intensity of N in lp-2 is stronger than that in $\text{NH}_2\text{-MIL-88B(Fe)}$, which can be attributed to the additional N from $\text{g-C}_3\text{N}_4$ in the lp-2 composite. As shown in Fig. 4(b), the C 1s spectrum of lp-2 was deconvoluted to six peaks located at 284.6 , 284.7 , 284.9 , 286.1 , 288.3 , and 288.9 eV . Specifically, the peaks at 284.6 eV and 284.7 eV can be attributed to C–C and C–H bands, consistent with those reported in the literature [48]. The peaks at 286.1 and 288.3 eV can be assigned to the C–N–C and C–(N)₃ groups of $\text{g-C}_3\text{N}_4$, respectively [49]. The rest two peaks at 284.9 and 288.9 eV [50] can be assigned to the benzoic ring and the carboxylate group (O=C=O) of the BDC–NH₂ linker from $\text{NH}_2\text{-MIL-88B(Fe)}$. Fig. 4c presents the XPS spectrum of N 1s for the lp-2 composite. The peak can be deconvoluted to four peaks at 397.7 , 398.9 , 399.8 and 401.1 eV , corresponding to the characteristic peaks for Fe–N, C–N=C, N–(C)₃ and –NH₂ or =NH of uncondensed terminal amino groups, respectively [1,13,48,51,52]. The Fe 2p XPS spectra was shown in Fig. 4d. The peaks at 712.4 and 726.2 eV with a satellite signal at 717.1 eV suggested the presence of Fe³⁺ in $\text{NH}_2\text{-MIL-88B(Fe)}$ [42]. In contrast, its binding energy had a slight shift of 0.4 eV (to 712.0 and 725.8 eV , respectively) in the lp-2 composite. This negative shift can be attributed to the increased electron density on Fe³⁺, likely because of the electron donation from the lone pair of electrons in the neighboring N atom in $\text{g-C}_3\text{N}_4$ to the Fe³⁺ site in $\text{NH}_2\text{-MIL-88B(Fe)}$, supported by the above-mentioned Fe–N band in the N 1s spectrum (Fig. 4(c)) [52,53]. The XPS results further indicated the neighboring interaction between $\text{g-C}_3\text{N}_4$ and $\text{NH}_2\text{-MIL-88B(Fe)}$ in the lp-2 composite, consistent with the TEM analyses.

UV-vis DRS was conducted to estimate the optical property of the samples. As shown in Fig. 5, the parent $\text{NH}_2\text{-MIL-88B(Fe)}$ has a broad intense absorption in the visible region, which can be

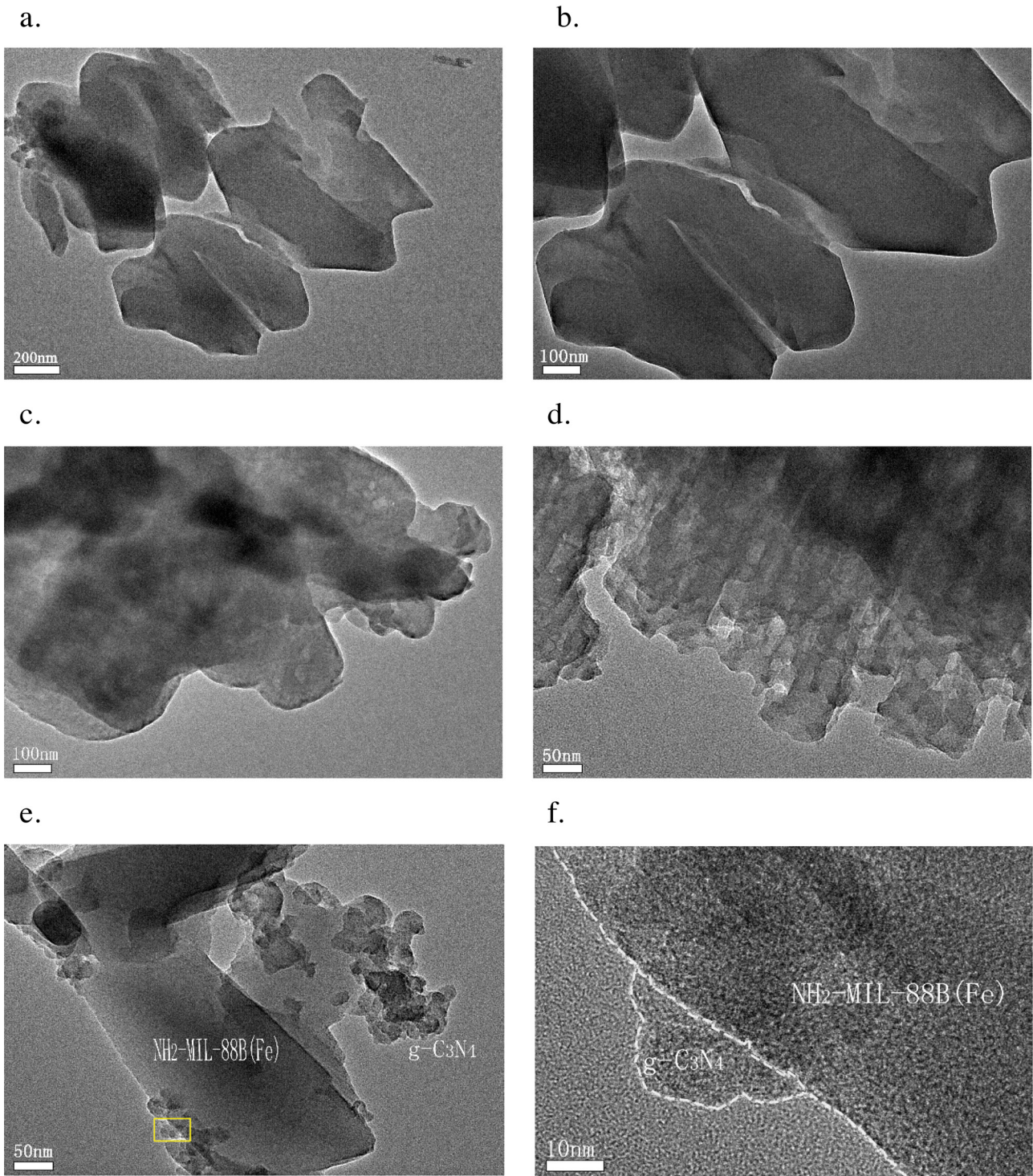


Fig. 3. TEM images of (a, b) NH₂-MIL-88(Fe), (c, d) g-C₃N₄, and (e)lp-2. HRTEM image of lp-2 Zoomed-in Fig. 3e (f).

ascribed to the presence of Fe₃O clusters in NH₂-MIL-88B(Fe), and further enhanced by the –NH₂ group attached to the BDC linker [42,54]. Meanwhile, the absorption at the wavelength of <450 nm could be attributed to the band gap of g-C₃N₄ [55]. Highly similar hybridized spectra are noticed in all the lp-x composites, which can be deconvoluted to two bands, one is threshold at ca. 450 nm belonging to the g-C₃N₄, and the other is at ca. 800 nm belonging to the NH₂-MIL-88B(Fe). Moreover, as the added amount of g-C₃N₄ in the lp-x composites increases, the intensity of the absorp-

tion band at 450 nm decrease, since the NH₂-MIL-88B(Fe) shows stronger absorption.

The band gap energy (E_g) is estimated according to the Tauc plot approach [56]:

$$K(hv - E_g)^{1/n} = F(R)hv$$

where K is a constant, F(R) is the absorption coefficient, and n is determined by the type of optical transition of the samples.

The plots of $(hv)^{1/2}$ versus photon energy (hv) are displayed in the inset of Fig. 5. The E_g of the parent NH₂-MIL-88B(Fe) and g-C₃N₄

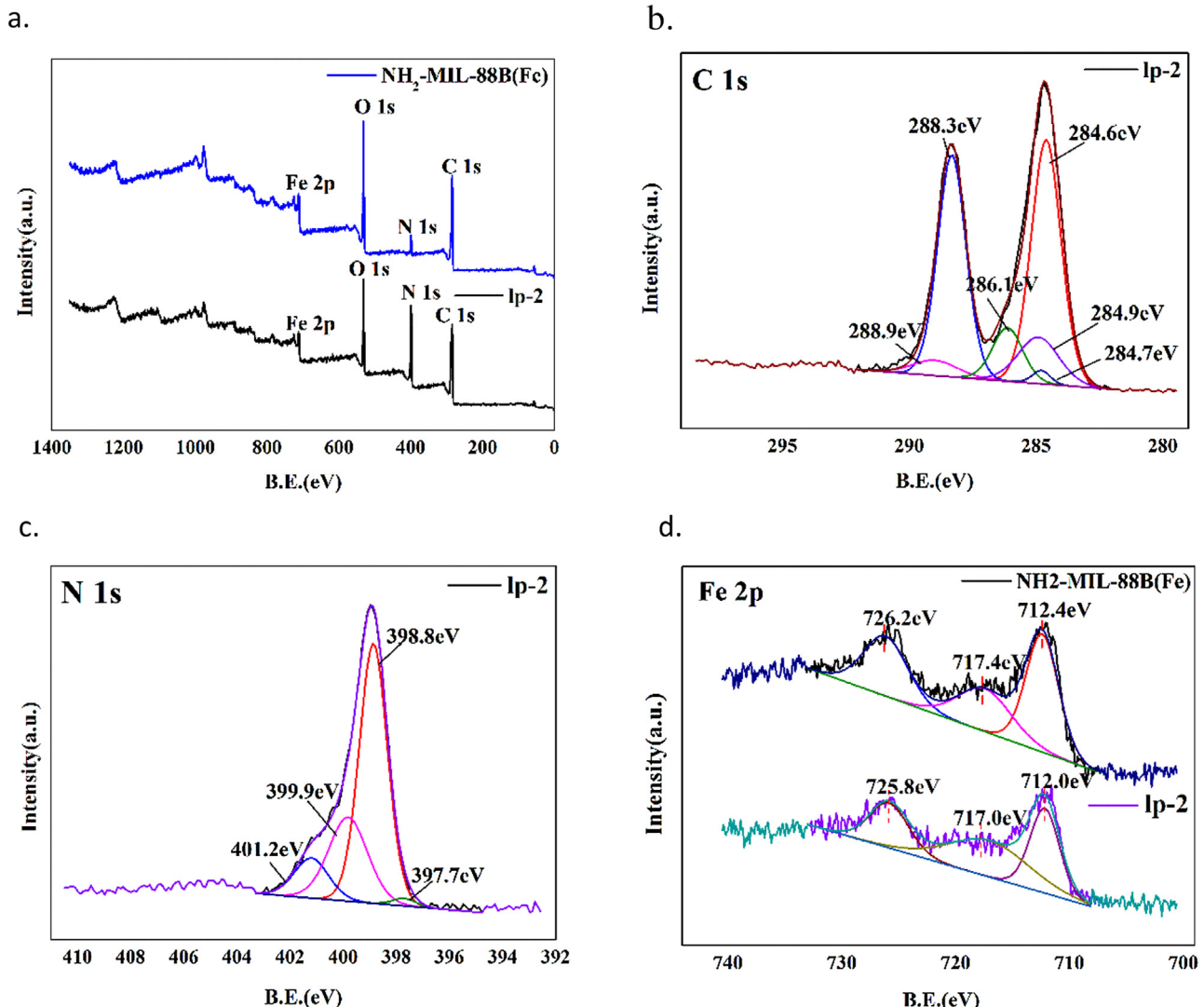


Fig. 4. XPS spectra of lp-2 referred to the parent NH₂-MIL-88B(Fe): (a) survey scan, (b) C 1s, (c) N 1s, and (d) Fe 2p.

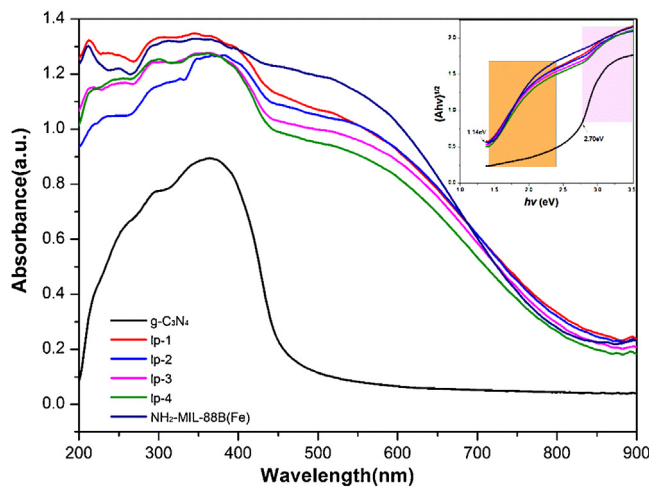


Fig. 5. UV-vis spectra of lp-x composites referred to the parent NH₂-MIL-88B(Fe) and g-C₃N₄. (Inset. Plots of $(\Delta A \Delta \nu)^{1/2}$ vs. photon energy (hv)).

were estimated to be 1.14 and 2.70 eV, respectively. In contrast, the above two E_g edges located at 1.14 and 2.70 eV can be observed for all the lp-x composites, suggesting the successful hybridization

[41,42] of g-C₃N₄ and NH₂-MIL-88B(Fe), resulting in the formation of heterojunction between NH₂-MIL-88B(Fe) and g-C₃N₄.

3.2. MB degradation of the lp-x composites

Photodegradation of MB was carried out under irradiation by visible light to identify the contribution of lp-x heterojunctions on the separation of charge carriers. As illustrated in Fig. 6, The MB degradation followed the order of lp-2 > lp-1 > NH₂-MIL-88(Fe) > lp-3 > lp-4 > g-C₃N₄. The MB degradation reached 24.8% and 57.0% of MB within 120 min on the parent g-C₃N₄ and NH₂-MIL-88B(Fe), respectively. In contrast, all of the lp-x composites exhibit higher MB degradation than that of both parent samples, indicating the presence of the synergistic effect between NH₂-MIL-88(Fe) and g-C₃N₄ as a heterojunction. More significantly, the MB degradation of the lp-2 composite reached 100%, which is almost twice of that of the parent NH₂-MIL-88B(Fe) and 4 times higher than that of the parent g-C₃N₄, indicating synergistic effect of the heterojunction of g-C₃N₄ and NH₂-MIL-88B(Fe) on improving the MB photodegradation is strong on the lp-2 composite. The much higher MB degradation can be attributed to the efficient electron transfer from g-C₃N₄ to NH₂-MIL-88(Fe) for the facilitation of Fenton-like excitation of H₂O₂, which will be further discussed

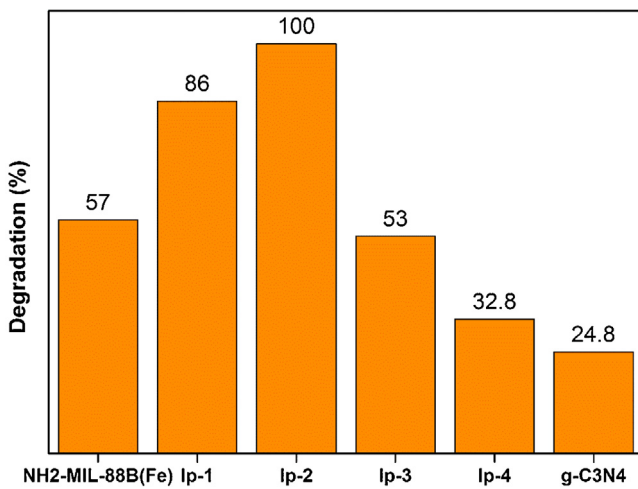


Fig. 6. Degradation of MB over Ip-x composites referred to NH₂-MIL-88B(Fe) and g-C₃N₄ in 120 min. (Reaction conditions: 50 mg of photocatalyst, 50 mL of 30 mg/L MB, 100 μ L of H₂O₂, pH of 7).

extensively in the following session. It should also be noted that excessive loading of g-C₃N₄ upon NH₂-MIL-88B(Fe) (Ip-3 and Ip-4) results in decreased MB degradation, which is likely due to the

“covering effect” [57] (further elaborated in the latter session). Therefore, appropriate loading of g-C₃N₄ is required to achieve the optimal MB degradation of Ip-x composites.

Control experiments were carried out to clarify the contribution of different parameters on the photodegradation. Fig. 7(a) displays the concentration (C/C_0) changes of MB versus time under different conditions. No decomposition of MB is observed irradiated by visible light for 120 min, indicating MB remains stable in water without H₂O₂ and photocatalyst. The degradation efficiency of MB reaches 18% in 120 min with the addition of H₂O₂, confirming that H₂O₂ could mildly degrade MB under visible light without photocatalyst. Ip-2 alone without H₂O₂ shows tiny degradation of MB, which could be attributed to the superoxide radical from photoelectron and oxygen molecule from air^{32b}. Moreover, Ip-2 in the presence of H₂O₂ shows 36.5% of MB degradation under dark condition, indicating Ip-2 could act as a mild Fenton-like photocatalyst for MB degradation, similar as Fe₃O₄ [58], α -FeOOH [59], and Fe-ZSM-5 zeolite [60]. In sharp contrast, almost 100% of MB degradation was achieved in 120 min, when using Ip-2 with H₂O₂ irradiated by visible light, confirmed in the UV-vis absorption spectral variation of MB in Fig. 7(b). Therefore, the MB degradation efficiency is contributed from the synergetic effect between Ip-2 and H₂O₂ under visible light, likely through Fenton-like reaction. It should be mentioned that the photo-sensitization effect from colorful pollutants

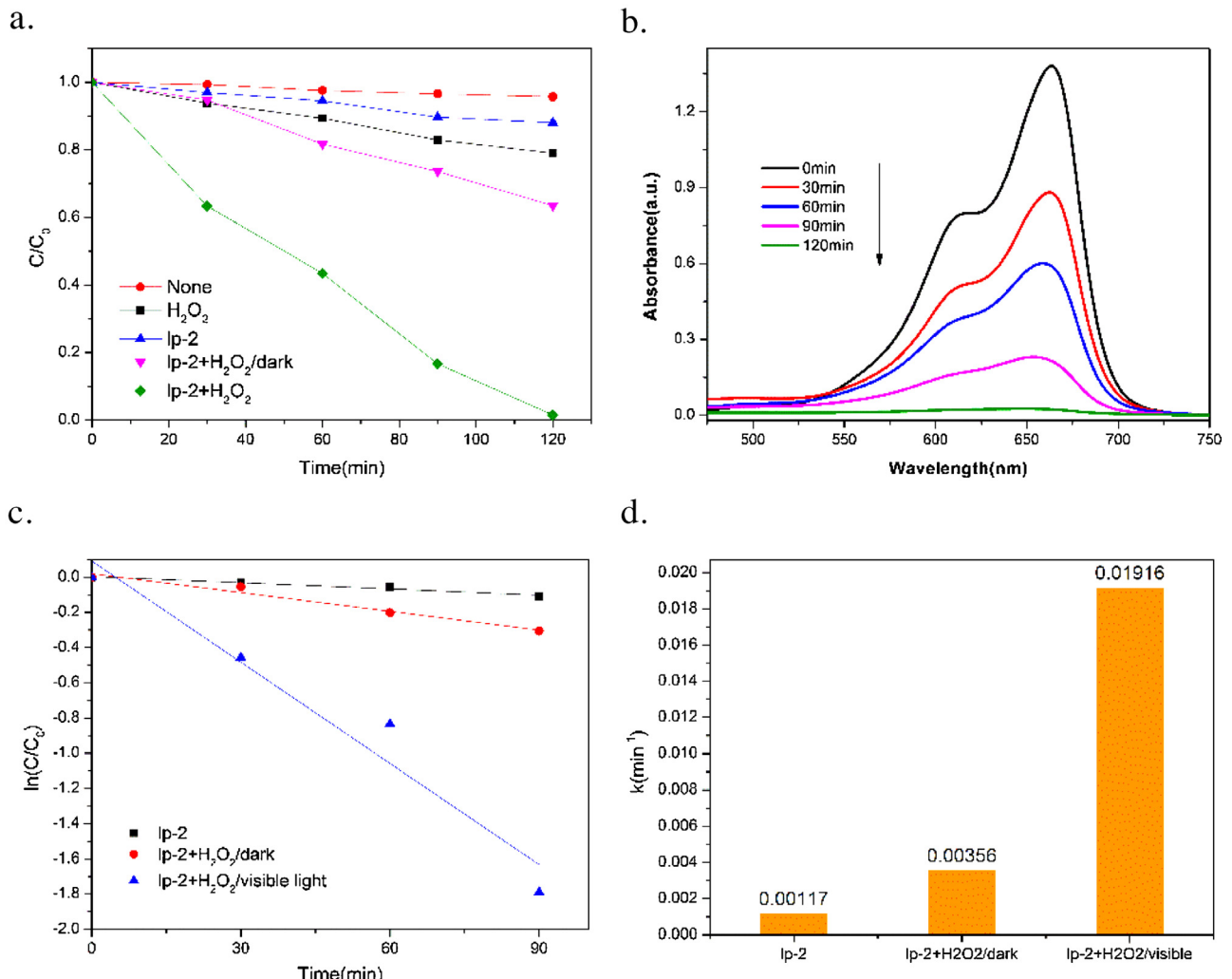


Fig. 7. (a) Degradation of MB under different conditions. (b) The UV-vis spectral changes of MB with time. (c) Pseudo-first-order kinetics curves of the degradation of MB under different conditions. (d) Comparison of the apparent reaction rate constants of the degradation of MB under different conditions. (Reaction conditions: 50 mg photocatalyst, 50 mL of MB at 30 mg/L, 100 μ L of H₂O₂, pH of 7).

[61] was ruled out by using colorless salicylic acid as the probe for photocatalytic degradation (Fig. S1).

To quantify the synergistic effect of lp-2 photocatalyst and H_2O_2 under visible light, the kinetic curves for MB photodegradation are well fitted to the pseudo-first order model ($\ln(\text{C}/\text{C}_0) = kt$) (Fig. 7(c)), where k for different reactions are listed in Fig. 7(d). The rate constant (k) of the lp-2/visible light/ H_2O_2 system (0.01916 min^{-1}) is higher than that of the lp-2/dark/ H_2O_2 (0.00356 min^{-1}) system, suggesting the presence of visible light facilitates the MB degradation greatly. The synergistic effect for the lp-2/visible light/ H_2O_2 system was estimated by synergistic index (SI) [26], $\text{SI} = k_{\text{MVH}}/(k_{\text{MH}} + k_{\text{MV}})$, in which k_{MVH} , k_{MH} , and k_{MV} are the rate constants about the systems of lp-2/visible light/ H_2O_2 , lp-2/visible light and lp-2/dark/ H_2O_2 , respectively. The SI of the lp-2/visible light/ H_2O_2 system was calculated to be 4.05, that is to say, the enhancement of the synergistic effect of lp-2/visible light/ H_2O_2 was 305%, much greater than that of MIL-53(Fe) (122% [26]). Therefore, the results indicate that the incorporation of $\text{g-C}_3\text{N}_4$ can dramatically enhance the SI of MOFs.

Water stability of MOFs and MOF-based materials is a great concern for the further application of such materials in various fields^{7b}. The stability of lp-2 was evaluated in the recycling experiments. The lp-2 was regenerated by simple filtration followed with drying of the spent photocatalyst at 60°C . The MB degradation of lp-2 in multiple runs is shown in Fig. 8. Almost no loss of MB photodegradation

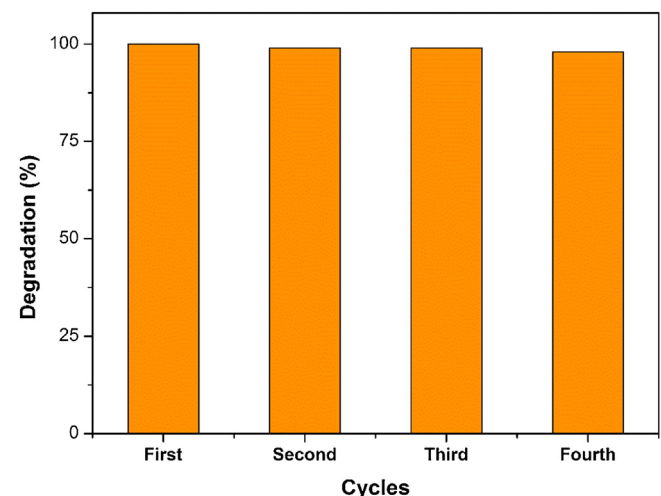


Fig. 8. Degradation of MB over lp-2 composite at multiple regeneration cycles. (Reaction conditions: 50 mg photocatalyst, 50 mL of MB at 30 mg/L, 100 μL of H_2O_2 , pH of 7).

at all was observed on lp-2 after four runs, suggesting the lp-2 photocatalyst exhibited excellent regenerability MB photodegradation as well as stability in aqueous solution. XRD characterization of lp-2 after multiple cyclic usages was carried out. As shown in Fig. S2,

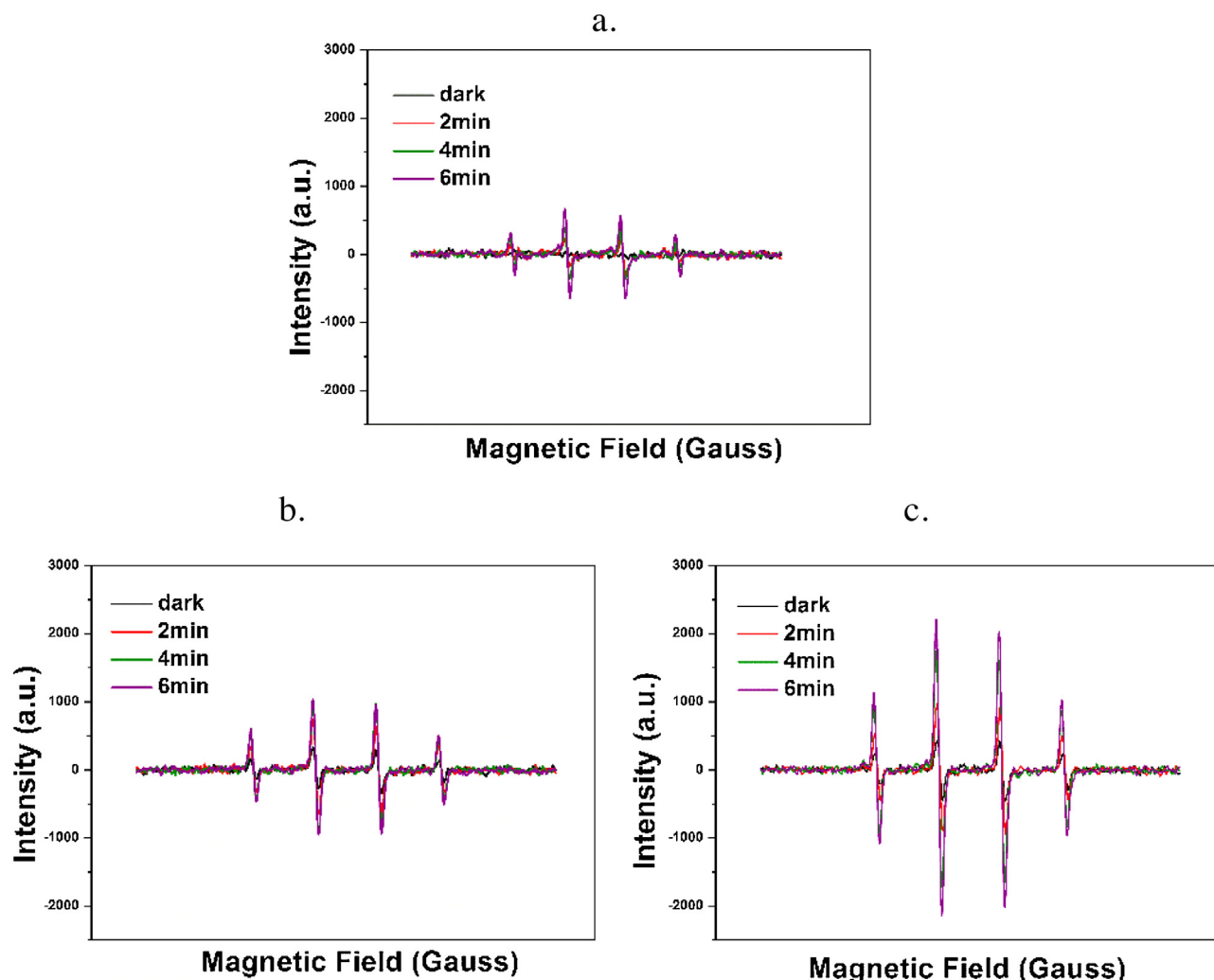


Fig. 9. ESR spectra of DMPO-•OH adducts formed with irradiation time of visible light in the suspension of (a) lp-2, (b) $\text{NH}_2\text{-MIL-88B(Fe)}/\text{H}_2\text{O}_2$, and (c) lp-2/ H_2O_2 .

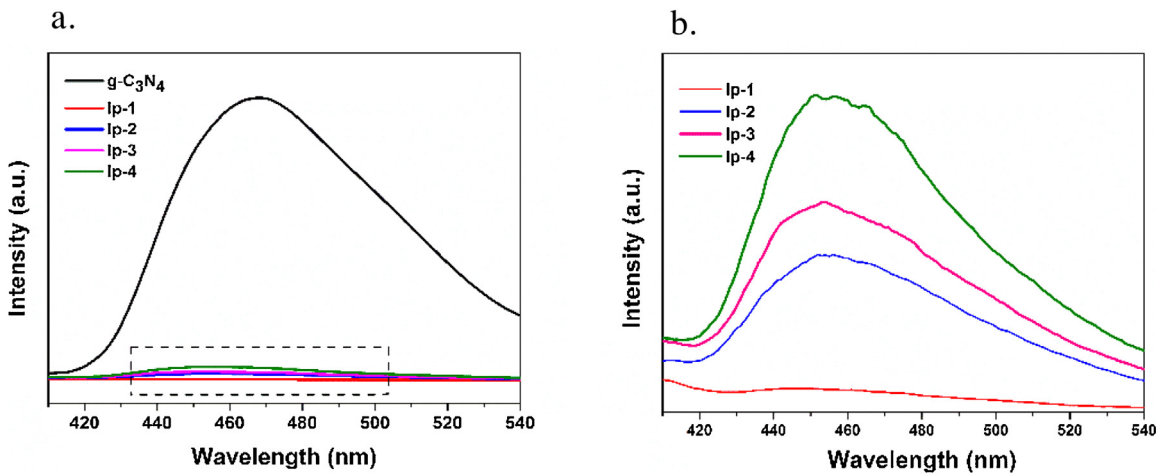


Fig. 10. (a) PL emission spectra of lp-x composites referred to g-C₃N₄; (b) Zoomed-in PL spectra of lp-x composites.

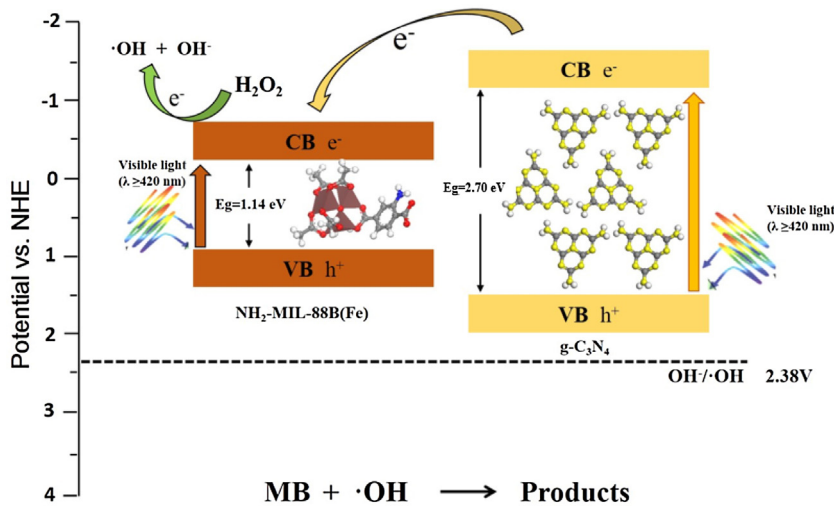


Fig. 11. Mechanistic scheme of the lp-2 composite for the photocatalytic degradation of MB with H₂O₂ under visible light.

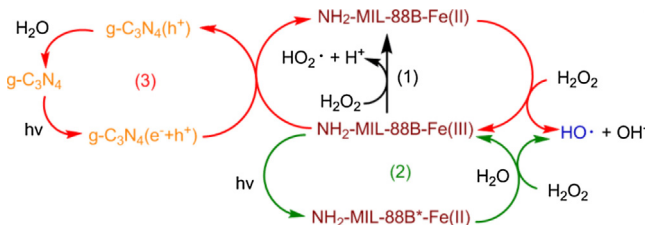
except the fresh lp-2 (with slight change on the peak intensity), the ones after cyclic usages showed similar XRD patterns. Worth noting the NH₂-MIL-88B(Fe) framework has been reported as a flexible MOF with interesting “breathing effect”. The crystalline structure of NH₂-MIL-88B(Fe) changes slightly when applying external stimuli (i.e., solvent [62]), due to the host-guest interaction, reported by Kitagawa et al. [63]. Here in the synthesis of fresh lp-2, the solvent used was MeOH and DMF, while the degradation solution created a different environment, inducing the slight change of the MOF structure (indicated in the XRD patterns in Fig. S2). Overall, after adapted to the new environment, the photocatalyst structure of lp-2 remained unchanged after cyclic usage, suggesting excellent stability of lp-2 for photocatalytic degradation of MB. This is more superior than most of MOFs-based photocatalysts reported so far [64–66].

3.3. Proposed photocatalytic mechanism

The ·OH radical from H₂O₂ excitation accounts for the effectiveness of Fenton-like photocatalyst for MB photodegradation, which can be quantified by ESR techniques using DMPO as a trapping reagent. The stronger the intensity, the larger is the generated ·OH amount. The synergistic effect between NH₂-MIL-88B(Fe) and g-C₃N₄ on ·OH generation was shown in Fig. 9. With irradiation time

prolonged, the characteristic quartet peaks of DMPO-·OH adduct [67] with intensity ratio of ca. 1:2:2:1 can be observed, indicating the photocatalytic potential of the as-prepared samples. The amount of generated ·OH follows the order of lp-2 + H₂O₂ > NH₂-MIL-88B(Fe) + H₂O₂ > lp-2. The flat band of NH₂-MIL-88B(Fe) is approximately 0.13 eV versus NHE, while the CB of g-C₃N₄ is ca -1.14 eV versus NHE [41,42]. The band gap of NH₂-MIL-88B(Fe) and g-C₃N₄ are 1.14 and 2.70 eV, respectively, estimated from the UV-DRS spectroscopy in Fig. 5. Thus, the VB positions of NH₂-MIL-88B(Fe) and g-C₃N₄ are estimated to 1.27 and 1.56 eV versus NHE, respectively. As the potential of OH⁻/·OH (2.3 eV vs NHE) is more positive than both NH₂-MIL-88B(Fe) and g-C₃N₄ (Fig. 11), negligible ·OH can be generated on the surface of lp-2 without H₂O₂ addition under visible light, consistent with the negligible amount of generated ·OH in Fig. 9. With the addition of H₂O₂, the amount of generated ·OH increased dramatically, which can be ascribed to the Fenton-like excitation of H₂O₂ for ·OH generation. More importantly, compared with NH₂-MIL-88B(Fe) + H₂O₂, lp-2 + H₂O₂ exhibits stronger ·OH intensity, suggesting the synergy between g-C₃N₄ and NH₂-MIL-88B(Fe) on the Fenton-like excitation of H₂O₂ for ·OH generation is present.

The PL analyses were used to investigate the transfer of the photo-induced electrons between g-C₃N₄ and NH₂-MIL-88B(Fe). Fig. 10 shows the PL spectra of the lp-x composites referred to



Scheme 1. Illustration of Fenton-like excitation of H_2O_2 for $\cdot\text{OH}$ generation under visible light.

the parent $\text{g-C}_3\text{N}_4$. A magnificent band was observed for the parent $\text{g-C}_3\text{N}_4$, as $\text{g-C}_3\text{N}_4$ itself can be excited as a photocatalyst with large recombination rate of photo-generated electron-hole pairs [66]. In sharp contrast, all the lp-x composites exhibit quite low PL intensity, suggesting little charge recombination occurred after hybridizing $\text{NH}_2\text{-MIL-88B(Fe)}$ with $\text{g-C}_3\text{N}_4$. The difference suggests that the portion of $\text{NH}_2\text{-MIL-88B(Fe)}$ in lp-x composites suppressed the recombination of the photogenerated carrier. That is to say, the photogenerated electrons on $\text{g-C}_3\text{N}_4$ can effectively transfer to the $\text{NH}_2\text{-MIL-88B(Fe)}$ with less charge recombination, resulting in the formation of more activated $\cdot\text{OH}$ for the MB degradation. Moreover, for different lp-x samples, the PL intensity decreases with increase in the amount of $\text{NH}_2\text{-MIL-88B(Fe)}$ in lp-x composites, as shown in Fig. 10(b). The trend further confirmed the role of hybridized $\text{NH}_2\text{-MIL-88B(Fe)}$. The significantly suppressed recombination of the photogenerated carrier on the lp-x composites indicated the formation of heterojunction between $\text{NH}_2\text{-MIL-88B(Fe)}$ and $\text{g-C}_3\text{N}_4$ [68], consistent with the XPS and TEM analyses. Additionally, the lp-3 and lp-4 shows weaker PL intensity than lp-2 , but lower MB degradation. This is likely due to the “covering effect” mentioned in 3.2. More specifically, (i) excessive $\text{g-C}_3\text{N}_4$ may lead to decreased surface active sites on $\text{NH}_2\text{-MIL-88B(Fe)}$; and (ii) excessive $\text{g-C}_3\text{N}_4$ may shield light absorption and generation of photo-generated electron by $\text{NH}_2\text{-MIL-88B(Fe)}$.

On the basis of the above clues, the paths for Fenton-like excitation of H_2O_2 for $\cdot\text{OH}$ generation over lp-2 are demonstrated in Scheme 1. Two primary mechanisms can be involved: (i) direct Fenton-like excitation of H_2O_2 (path (1)); and (ii) photo-induced Fenton-like excitation of H_2O_2 (path (2) and (3)). (i) For direct Fenton-like excitation of H_2O_2 , H_2O_2 attacks Fe(III) in $\text{NH}_2\text{-MIL-88B(Fe)}$ to produce Fe(II) , which further activates H_2O_2 through Fenton-like reaction to generate $\cdot\text{OH}$ radicals [26], and the MOF itself is oxidized to the original state, forming a cyclic loop. It should be noticed that $\text{lp-2} + \text{H}_2\text{O}_2$ and $\text{NH}_2\text{-MIL-88B(Fe)} + \text{H}_2\text{O}_2$ systems can generate $\cdot\text{OH}$ even at dark condition (Fig. 9(a) and (b)). (ii) For photo-induced Fenton-like excitation of H_2O_2 , two different paths are involved. For path (2), Iron-centered MOFs, composed of Fe-oxo clusters, could jump to the excited state of MOF*, herein $\text{NH}_2\text{-MIL-88B*}(Fe)$ under visible light [26,27]. The photo-induced electrons in the organic linker transfer to the Fe-oxo clusters, similar as the excitation of electrons from the VB to the CB, results in the formation of Fe(II) [42]. Under such situation, the photo-induced electrons on CB could be captured and reacted with H_2O_2 to produce $\cdot\text{OH}$ via Fenton-like excitation of H_2O_2 . Here, the introduced $-\text{NH}_2$ to MIL-88B(Fe) is to enhance visible light absorption by increasing ligand-to-metal charge transfer (LMCT) [69]. For path (3), when $\text{g-C}_3\text{N}_4$ was introduced to $\text{NH}_2\text{-MIL-88B(Fe)}$, $\text{g-C}_3\text{N}_4$ itself can be excited as a photocatalyst firstly, the photo-generated electrons were transfer from $\text{g-C}_3\text{N}_4$ to $\text{NH}_2\text{-MIL-88B(Fe)}$ to form Fe(II) , which further facilitated the Fenton-like activation of H_2O_2 in path (1) loop. Therefore, with the efficient electron transfer from $\text{g-C}_3\text{N}_4$ to $\text{NH}_2\text{-MIL-88B(Fe)}$, the electron-hole recombination on $\text{g-C}_3\text{N}_4$ can be reduced, consistent with the experiment results in Fig. 10. It should be mentioned that the degradation of MB in dark is slower

than that under visible light, since the rate constant of the $\text{lp-2}/\text{visible light}/\text{H}_2\text{O}_2$ system is higher than $\text{lp-2}/\text{dark}/\text{H}_2\text{O}_2$ system (Fig. 7d), thus the photo-induced mechanism could be ruled out, which is supported by the ESR results.

To sum up, the mechanistic scheme of the lp-2 composite for the photocatalytic degradation of MB with H_2O_2 irradiated by visible light is illustrated in Fig. 11. Under irradiation, the electrons of $\text{NH}_2\text{-MIL-88B(Fe)}$ and $\text{g-C}_3\text{N}_4$ were excited from the VB to the CB. Subsequently, the photo-induced electron of Fenton-like $\text{NH}_2\text{-MIL-88B(Fe)}$ photocatalyst reacts with H_2O_2 to generate $\cdot\text{OH}$. Meanwhile, the excited electron at the CB of $\text{g-C}_3\text{N}_4$ is transferred to the CB of $\text{NH}_2\text{-MIL-88B(Fe)}$ and induces the Fenton-like reaction. Therefore, with the formation of $\text{g-C}_3\text{N}_4/\text{NH}_2\text{-MIL-88B(Fe)}$ heterojunction, the active $\cdot\text{OH}$ can be generated effectively via the Fenton-like excitation of H_2O_2 , resulting in dramatically enhanced MB photodegradation under visible light.

4. Conclusion

Highly active $\text{g-C}_3\text{N}_4/\text{NH}_2\text{-MIL-88B(Fe)}$ Fenton-like heterojunction photocatalysts were successfully fabricated for the effective MB photodegradation under visible light. The MB degradation of the lp-2 composite reach almost 100% after 120 min, which is around 2 and 4 times higher than that of the parent $\text{NH}_2\text{-MIL-88B(Fe)}$ and $\text{g-C}_3\text{N}_4$, respectively. The $\text{lp-2}/\text{visible light}/\text{H}_2\text{O}_2$ system showed an amplified synergistic index (SI) of 305%. Characterization results suggests the successful hybridization of $\text{g-C}_3\text{N}_4$ and $\text{NH}_2\text{-MIL-88B(Fe)}$ and the formation of the $\text{g-C}_3\text{N}_4/\text{NH}_2\text{-MIL-88B(Fe)}$ heterojunction in the lp-x composites. The enhanced activity of the lp-x composites can be attributed to the facilitated Fenton-like excitation of H_2O_2 via dramatically enhanced transfer of photo-induced electrons, due to the formation of the $\text{g-C}_3\text{N}_4/\text{NH}_2\text{-MIL-88B(Fe)}$ heterojunction. Mechanistically, in the Fenton-like reaction system, electrons are excited from the VB to the CB in both $\text{g-C}_3\text{N}_4$ and $\text{NH}_2\text{-MIL-88B(Fe)}$, then the electrons on the CB of $\text{g-C}_3\text{N}_4$ are transferred to the CB of $\text{NH}_2\text{-MIL-88B(Fe)}$ and avoided the recombination of photogenerated $\text{e}^- + \text{h}^+$ pairs on $\text{g-C}_3\text{N}_4$, supported by the PL analysis. Therefore, the heterojunction of $\text{g-C}_3\text{N}_4$ and $\text{NH}_2\text{-MIL-88B(Fe)}$ facilitated Fenton-like excitation of H_2O_2 to form $\cdot\text{OH}$, consolidated by electron spin resonance result. Additionally, the lp-x composite demonstrates excellent reusability and stability after cyclic usage. The excellent photocatalytic performance and regenerability make the lp-x composites a type of promising heterojunction photocatalysts for Fenton-like excitation of H_2O_2 under visible light. The application of $\text{g-C}_3\text{N}_4$ to hybridize MOFs can be a potential approach to construct efficient heterojunction for visible light-induced photodegradation and worthy of further investigation.

Acknowledgements

The financial supports received from Guangdong Natural Science Funds for Distinguished Young Scholar (2016A030306031), the National Natural Science Foundation of China (21576093), the Guangdong Program for Support of Top-notch Young Professionals (2015TQ01N327), and Pearl River and S&T Nova Program of Guangzhou (201610010039) are gratefully acknowledged.

Appendix A. Supplementary data

Supplementary data associated with this article can be found, in the online version, at <http://dx.doi.org/10.1016/j.apcatb.2016.09.073>.

References

- [1] Y.Q. Wang, X.J. Yu, D.Z. Sun, Synthesis, characterization, and photocatalytic activity of $TiO_{(2-x)}N_{(x)}$ nanocatalyst, *J. Hazard. Mater.* 144 (2007) 328–333.
- [2] Y. Luan, N.Y. Zheng Qi, J. Tang, G. Wang, Merging metal–organic framework catalysis with organocatalysis: a thiourea functionalized heterogeneous catalyst at the nanoscale, *Environ. Sci. Technol.* 4 (2014) 925.
- [3] M.N. Chong, B. Jin, C.W. Chow, C. Saint, Recent developments in photocatalytic water treatment technology: a review, *Water Res.* 44 (2010) 2997–3027.
- [4] D.H. Bremner, R. Molina, F. Martínez, J.A. Melero, Y. Segura, Degradation of phenolic aqueous solutions by high frequency sono-fenton systems (US– Fe_2O_3 /SBA-15– H_2O_2), *Appl. Catal. B: Environ.* 90 (2009) 380–388.
- [5] M.I. Litter, Heterogeneous photocatalysis: Transition metal ions in photocatalytic systems, *Appl. Catal. B: Environ.* 23 (1999) 89–114.
- [6] G. Li, Z. Wang, M. Yu, Z. Quan, J. Lin, Fabrication and optical properties of core–shell structured spherical $SiO_2@GdVO_4$: Eu^{3+} phosphors via sol–gel process, *J. Solid State Chem.* 179 (2006) 2698–2706.
- [7] G.Z. Li, M. Yu, Z.L. Wang, J. Lin, R.S. Wang, J. Fang, Sol–gel fabrication and photoluminescence properties of $SiO_2@Gd_2O_3$: Eu^{3+} core–shell particles, *J. Nanosci. Nanotechnol.* 6 (2006) 1416–1422.
- [8] J. Lu, J.X. Lin, X.L. Zhao, R. Cao, Photochromic hybrid materials of cucurbituril and polyoxometalates as photocatalysts under visible light, *Chem. Commun. (Camb.)* 48 (2012) 669–671.
- [9] S.T.M. Michael, R. Hoffmann, Wonyong Choi, W. Detlef Bahnemann, Environmental applications of semiconductor photocatalysis, *Chem. Rev.* 95 (1995) 69–96.
- [10] J. Tracy, L. Thompson, John T. Yates, Surface science studies of the photoactivation of TiO_2 s new photochemical processes, *Chem. Rev.* 106 (2006) 4428–4453.
- [11] W. Liu, Z. Ai, L. Zhang, Design of a neutral three-dimensional electro-fenton system with foam nickel as particle electrodes for wastewater treatment, *J. Hazard. Mater.* 243 (2012) 257–264.
- [12] Alok D. Bokare, Wonyong Choi, Chromate-induced activation of hydrogen peroxide for oxidative degradation of aqueous organic pollutants, *Environ. Sci. Technol.* 44 (2010) 7232–7237.
- [13] X. Li, Y. Pi, Q. Xia, Z. Li, J. Xiao, TiO_2 encapsulated in salicylaldehyde– NH_2 –MIL-101(Cr) for enhanced visible light–driven photodegradation of MB, *Appl. Catal. B: Environ.* 191 (2016) 192–201.
- [14] M. Ge, L. Liu, W. Chen, Z. Zhou, Sunlight–driven degradation of Rhodamine B by peanut-shaped porous $BiVO_4$ nanostructures in the H_2O_2 –containing system, *CrystEngComm* 14 (2012) 1038–1044.
- [15] M. Su, C. He, V.K. Sharma, M. Abou Asi, D. Xia, X.Z. Li, H. Deng, Y. Xiong, Mesoporous zinc ferrite: synthesis characterization, and photocatalytic activity with H_2O_2 /visible light, *J. Hazard. Mater.* 211–212 (2012) 95–103.
- [16] C. Wang, D. Liu, W. Lin, Metal–organic frameworks as a tunable platform for designing functional molecular materials, *J. Am. Chem. Soc.* 135 (2013) 13222–13234.
- [17] P. Horcada, C. Serre, G. Maurin, N.A. Ramsahye, F. Balas, M. Vallet-Regí, M. Sebban, F. Taulelle, G. Férey, Flexible porous metal–organic frameworks for a controlled drug delivery, *J. Am. Chem. Soc.* 130 (2008) 6774–6780.
- [18] M. Alvaro, E. Carbonell, B. Ferrer, F.X. Llabres i Xamena, H. Garcia, Semiconductor behavior of a metal–organic framework (MOF), *Chemistry* 13 (2007) 5106–5112.
- [19] T.R. Cook, Y.R. Zheng, P.J. Stang, Metal–organic frameworks and self-assembled supramolecular coordination complexes: comparing and contrasting the design, synthesis, and functionality of metal–organic materials, *Chem. Rev.* 113 (2013) 734–777.
- [20] T. Zhang, W. Lin, Metal–organic frameworks for artificial photosynthesis and photocatalysis, *Chem. Soc. Rev.* 43 (2014) 5982–5993.
- [21] C.G. Silva, A. Corma, H. García, Metal–organic frameworks as semiconductors, *J. Mater. Chem.* 20 (2010) 3141–3156.
- [22] D. Wang, M. Wang, Z. Li, Fe-based metal–organic frameworks for highly selective photocatalytic benzene hydroxylation to phenol, *ACS Catal.* 5 (2015) 6852–6857.
- [23] S. Abedi, A. Morsali, Ordered mesoporous metal–organic frameworks incorporated with amorphous TiO_2 As photocatalyst for selective aerobic oxidation in sunlight irradiation, *ACS Catal.* 4 (2014) 1398–1403.
- [24] W.T. Sun, Q.Q. Meng, L.Q. Jing, D.N. Liu, Y. Cao, Facile synthesis of surface-modified nanosized α - Fe_2O_3 as efficient visible photocatalysts and mechanism insight, *J. Phys. Chem. C* 117 (2013) 1358–1365.
- [25] H. Hattori, Y. Ide, S.H. Ogo, K. Inumaru, M. Sadakane, T. Sano, Efficient and selective photocatalytic cyclohexane oxidation on a layered titanate modified with iron oxide under sunlight and CO_2 atmosphere, *ACS Catal.* 2 (2012) 1910–1915.
- [26] L. Ai, C. Zhang, L. Li, J. Jiang, Iron terephthalate metal–organic framework: revealing the effective activation of hydrogen peroxide for the degradation of organic dye under visible light irradiation, *Appl. Catal. B: Environ.* 148–149 (2014) 380–388.
- [27] K.G. Laurier, F. Vermoortele, R. Ameloot, D.E. De Vos, J. Hofkens, M.B. Roeffaers, Iron(III)-based metal–organic frameworks as visible light photocatalysts, *J. Am. Chem. Soc.* 135 (2013) 14488–14491.
- [28] J. Zhang, Y. Chen, X. Wang, Two-dimensional covalent carbon nitride nanosheets: synthesis, functionalization, and applications, *Energy Environ. Sci.* 8 (2015) 3092–3108.
- [29] Y. Zheng, L. Lin, B. Wang, X. Wang, Graphitic carbon nitride polymers toward sustainable photoredox catalysis, *Angew. Chem. Int. Ed. Engl.* 54 (2015) 12868–12884.
- [30] Y. Cui, Z. Ding, X. Fu, X. Wang, Construction of conjugated carbon nitride nanoarchitectures in solution at low temperatures for photoredox catalysis, *Angew. Chem. Int. Ed. Engl.* 51 (2012) 11814–11818.
- [31] J. Zhang, M. Zhang, C. Yang, X. Wang, Nanospherical carbon nitride frameworks with sharp edges accelerating charge collection and separation at a soft photocatalytic interface, *Adv. Mater.* 26 (2014) 4121–4126.
- [32] G. Zhang, M. Zhang, X. Ye, X. Qiu, S. Lin, X. Wang, Iodine modified carbon nitride semiconductors as visible light photocatalysts for hydrogen evolution, *Adv. Mater.* 26 (2014) 805–809.
- [33] Z. Lin, X. Wang, Nanostructure engineering and doping of conjugated carbon nitride semiconductors for hydrogen photosynthesis, *Angew. Chem. Int. Ed. Engl.* 52 (2013) 1735–1738.
- [34] M. Xu, L. Han, S. Dong, Facile fabrication of highly efficient g - C_3N_4 / Ag_2O heterostructured photocatalysts with enhanced visible-light photocatalytic activity, *ACS Appl. Mater. Interfaces* 5 (2013) 12533–12540.
- [35] X.F. Lu, Q.L. Wang, D.L. Cui, Preparation and photocatalytic properties of g - C_3N_4 / TiO_2 hybrid composite, *J. Mater. Sci. Technol.* 26 (2010) 925–930.
- [36] Y. Wang, R. Shi, J. Lin, Y. Zhu, Enhancement of photocurrent and photocatalytic activity of ZnO hybridized with graphite-like C_3N_4 , *Energy Environ. Sci.* 4 (2011) 2922–2929.
- [37] S. Ye, L.-G. Qiu, Y.-P. Yuan, Y.-J. Zhu, J. Xia, J.-F. Zhu, Facile fabrication of magnetically separable graphitic carbon nitride photocatalysts with enhanced photocatalytic activity under visible light, *J. Mater. Chem. A* 1 (2013) 3008–3015.
- [38] K. Sridharan, T. Kuriakose, R. Philip, T.J. Park, Transition metal (Fe, Co and Ni) oxide nanoparticles grafted graphitic carbon nitrides as efficient optical limiters and recyclable photocatalysts, *Appl. Surf. Sci.* 308 (2014) 139–147.
- [39] Y. Liu, Y.-X. Yu, W.-D. Zhang, Photoelectrochemical study on charge transfer properties of nanostructured Fe_2O_3 modified by g - C_3N_4 , *Int. J. Hydrogen Energy* 39 (2014) 9105–9113.
- [40] X. Ye, Y. Cui, X. Qiu, X. Wang, Selective oxidation of benzene to phenol by Fe–CN/TS-1 catalysts under visible light irradiation, *Appl. Catal. B: Environ.* 152–153 (2014) 383–389.
- [41] S. Cao, J. Low, J. Yu, M. Jaroniec, Polymeric photocatalysts based on graphitic carbon nitride, *Adv. Mater.* 27 (2015) 2150–2176.
- [42] L. Shi, T. Wang, H. Zhang, K. Chang, X. Meng, H. Liu, J. Ye, An amine-functionalized iron(III) metal–organic framework as efficient visible–Light photocatalyst for Cr(VI) reduction, *Adv. Sci.* 2 (2015) 1–8.
- [43] N. Liédana, P. Lozano, A. Galve, C. Téllez, J. Coronas, The template role of caffeine in its one-step encapsulation in MOF NH_2 –MIL-88B(Fe), *J. Mater. Chem. A* 2 (2014) 1144–1151.
- [44] Q. Liu, Y. Guo, Z. Chen, Z. Zhang, X. Fang, Constructing a novel ternary Fe(III)/graphene/ g - C_3N_4 composite photocatalyst with enhanced visible–light driven photocatalytic activity via interfacial charge transfer effect, *Appl. Catal. B: Environ.* 183 (2016) 231–241.
- [45] P. Serra-Crespo, E. Gobechia, E.V. Ramos-Fernandez, J. Juan-Alcaniz, A. Martínez-Joaristi, E. Stavitski, C.E. Kirschock, J.A. Martens, F. Kapteijn, J. Gascon, Interplay of metal node and amine functionality in NH_2 –MIL-53: modulating breathing behavior through intra-framework interactions, *Langmuir* 28 (2012) 12916–12922.
- [46] M.M. Paradkar, J. Irudayaraj, A rapid FTIR spectroscopic method for estimation of caffeine in soft drinks and total methylxanthines in tea and coffee, *J. Food Sci.* 67 (2002) 2507–2511.
- [47] Q. Liu, T.X. Chen, Y.R. Guo, Z.G. Zhang, X.M. Fang, Ultrathin g - C_3N_4 nanosheets coupled with carbon nanodots as 2D/0D composites for efficient photocatalytic H_2 evolution, *Appl. Catal. B: Environ.* 193 (2016) 248–258.
- [48] N. Boonprakob, N. Wetchakun, S. Phanichphant, D. Waxler, P. Sherrell, A. Nattestad, J. Chen, B. Inceesungvorn, Enhanced visible–light photocatalytic activity of g - C_3N_4 / TiO_2 films, *J. Colloid Interface Sci.* 417 (2014) 402–409.
- [49] X. Zhou, F. Peng, H. Wang, H. Yu, Y. Fang, Carbon nitride polymer sensitized TiO_2 nanotube arrays with enhanced visible light photoelectrochemical and photocatalytic performance, *Chem. Commun. (Camb.)* 47 (2011) 10323–10325.
- [50] C. Zhang, L. Ai, J. Jiang, Graphene hybridized photoactive iron terephthalate with enhanced photocatalytic activity for the degradation of rhodamine B under visible light, *Ind. Eng. Chem. Res.* 54 (2015) 153–163.
- [51] Z. Guo, Z. Zhang, W. Zhang, L. Zhou, H. Li, H. Wang, C. Andreazza-Vignolle, P. Andreazza, D. Zhao, Y. Wu, Q. Wang, T. Zhang, K. Jiang, Color–switchable, emission–enhanced fluorescence realized by engineering C-dot@C-dot nanoparticles, *ACS Appl. Mater. Interfaces* 6 (2014) 20700–20708.
- [52] A.J. Wagner, G.M. Wolfe, D.H. Fairbrother, Reactivity of vapor–deposited metal atoms with nitrogen–containing polymers and organic surfaces studied by in situ XPS, *Appl. Surf. Sci.* 219 (2003) 317–328.
- [53] G.-S. Shao, T.-Y. Ma, X.-J. Zhang, T.-Z. Ren, Z.-Y. Yuan, Phosphorus and nitrogen co-doped titania photocatalysts with a hierarchical meso-/macroporous structure, *J. Mater. Sci.* 44 (2009) 6754–6763.
- [54] R.H. Deng, K. Wang, W.J. Liu, D.R. Sun, Z.H. Li, Fe-based MOFs for photocatalytic CO_2 reduction: role of coordination unsaturated sites and dual excitation pathways, *ACS Catal.* 4 (2014) 4254–4260.
- [55] H. Wang, X. Yuan, Y. Wu, G. Zeng, X. Chen, L. Leng, H. Li, Synthesis and applications of novel graphitic carbon nitride/metal–organic frameworks mesoporous photocatalyst for dyes removal, *Appl. Catal. B: Environ.* 174–175 (2015) 445–454.

[56] J. Tauc, R. Grigorovici, A. Vancu, Optical properties and electronic structure of amorphous germanium, *Phys. Status Solidi (B)* 15 (1966) 627–637.

[57] J. Jin, J. Yu, D. Guo, C. Cui, W. Ho, A hierarchical Z-scheme CdS-WO_3 photocatalyst with enhanced CO_2 reduction activity, *Small* 11 (2015) 5262–5271.

[58] L. Xu, J. Wang, Fenton-like degradation of 2,4-dichlorophenol using Fe_3O_4 magnetic nanoparticles, *Appl. Catal. B: Environ.* 123–124 (2012) 117–126.

[59] J. Deng, J. Jiang, Y. Zhang, X. Lin, C. Du, Y. Xiong, FeVO_4 as a highly active heterogeneous fenton-like catalyst towards the degradation of Orange II, *Appl. Catal. B: Environ.* 84 (2008) 468–473.

[60] M.B. Kasiri, H. Aleboyeh, A. Aleboyeh, Degradation of acid blue 74 using Fe-ZSM₅ zeolite as a heterogeneous photo-fenton catalyst, *Appl. Catal. B: Environ.* 84 (2008) 9–15.

[61] N. Barbero, D. Vione, Why dyes should not be used to test the photocatalytic activity of semiconductor oxides, *Environ. Sci. Technol.* 50 (2016) 2130–2131.

[62] M. Ma, I. Bétard, N.S. Al-Hokbany, R.A. Fischer, N. Metzler-Nolte, Iron-based metal-organic frameworks MIL-88B and NH₂-MIL-88B: high quality microwave synthesis and solvent-Induced lattice Breathing, *Cryst. Growth Des.* 13 (2013) 2286–2291.

[63] S. Kitagawa, R. Kitaura, S. Noro, Functional porous coordination polymers, *Angew. Chem. Int. Ed. Engl.* 43 (2004) 2334–2375.

[64] N. Mohaghegh, S. Kamrani, M. Tasviri, M. Elahifard, M. Gholami, Nanoporous Ag_2O photocatalysts based on copper terephthalate metal-organic frameworks, *J. Mater. Sci.* 50 (2015) 4536–4546.

[65] Q. Sun, M. Liu, K. Li, Y. Zuo, Y. Han, J. Wang, C. Song, G. Zhang, X. Guo, Facile synthesis of Fe-containing metal-organic frameworks as highly efficient catalysts for degradation of phenol at neutral pH and ambient temperature, *CrystEngComm* 17 (2015) 7160–7168.

[66] F.Y. Yi, J.P. Li, D. Wu, Z.M. Sun, A series of multifunctional metal-organic frameworks showing excellent luminescent sensing, sensitization, and adsorbent abilities, *Chemistry* 21 (2015) 11475–11482.

[67] E. Malka, I. Perelshtein, A. Lipovsky, Y. Shalom, L. Naparstek, N. Perkas, T. Patick, R. Lubart, Y. Nitzan, E. Banin, A. Gedanken, Eradication of multi-drug resistant bacteria by a novel Zn-doped CuO nanocomposite, *Small* 9 (2013) 4069–4076.

[68] G. Gao, Y. Jiao, F. Ma, Y. Jiao, E. Wacławik, A. Du, Carbon nanodot decorated graphitic carbon nitride: new insights into the enhanced photocatalytic water splitting from ab initio studies, *Phys. Chem. Chem. Phys.* 17 (2015) 31140–31144.

[69] D. Sun, Y. Fu, W. Liu, L. Ye, D. Wang, L. Yang, X. Fu, Z. Li, Studies on photocatalytic CO_2 reduction over NH₂-UiO-66(Zr) and its derivatives: towards better understanding of photocatalysis on metal-organic frameworks, *Chemistry* 19 (2013) 14279–14285.